Physica **67** (1973) 533–563 © *North-Holland Publishing Co.*

INELASTIC NON-VIOLENT HEAVY-ATOM COLLISIONS

D.J. BIERMAN and W.C. TURKENBURG

FOM-Institute for Atomic and Molecular Physics, Amsterdam, Nederland

Received 12 February 1973

Synopsis

Measurements are presented of inelastic energies dissipated during small-angle scattering of Ar^+ ions by Ar and Ne^+ by Ne. The primary energies range from 3.5 to 90 keV. In the secondary-energy spectrum of the projectiles typical structures are observed which are contributed to different possible excitation channels. An elastic peak and a peak due to excitation of the target atom are observed. Other peaks and details of the structure cannot be interpreted in an unique way. It may partly be explained by simultaneous excitation of projectile and target particle although excitation of projectile alone is not observed. However, for the inelastic energy spectra arising from Ne^+–Ne collisions in which the product of primary energy and scattering angle is larger than 10 keV deg no satisfactory explanation can be given in terms of well-defined excitations. Relative differential cross sections for elastic scattering show oscillations. These oscillations are caused by interference of partial waves scattered by different potentials.

Semiclassical calculations of elastic differential cross sections are presented. Instead of using the impact-parameter approximation, the "exact" orbits of the particles are calculated to obtain the phase shifts. Furthermore, using the same methods, the critical internuclear distance, at which the potentials cross which play a role in neon ($2p^5$,3s) excitation, is calculated as well as the inelastic differential cross section for the process $Ne^+ + Ne \rightarrow Ne^+ + Ne^*$ ($2p^5$,3s).

1. *Introduction.* The excitation and ionization of the partners in a single ion–atom collision reflect themselves in the decrease of the relative kinetic energy of the two particles. Therefore, the measurement of this energy loss can yield information about the various possible excitation channels, the relative probabilities of entering the different channels and the excitation mechanisms. During the last few years much attention has been paid to the measurement of the inelastic losses caused by violent heavy-ion–atom collisions, as a function of the distance of closest approach[1–9]). Structures in these energy-loss spectra have been observed which are attributed to distinct excitations of inner-shell electrons. A promotion mechanism for these inner-shell electrons has been proposed by Fano and Lichten[10,11]).

Processes in which only outer-shell penetration occurs have been studied too by means of inelastic energy-loss measurements. Lorentz and Aberth[12]) made an

energy analysis of a He^+ beam scattered from He. They observed structures in which they distinguished elastically and inelastically scattered particles. Because their main work was concerned with the measurement of elastic differential cross sections and the explanation of their oscillations, they did not investigate the inelastic part of the spectrum any further.

In a second paper[13]) energy spectra were also presented for He^+–Ne, He^+–Ar and Ar^+–Ar pairs. In all these cases structures were observed which could be correlated to excitations of an outer-shell electron(s) of the target or (and) projectile. Smith *et al.*[14]) introduced for this type of investigation the term "collision spectroscopy"; the main aim of this investigation being the calculation of potential parameters from the cross sections making conventional theoretical approximations.

Similar experiments with primary energies up to 3000 eV were performed by a French group in Orsay[15,16]). In that work not only elastic differential cross sections but also inelastic differential cross sections were measured. The excitation mechanism was described in terms of diabatic transitions which take place at the pseudo-crossing of two energy levels. Crossing points were determined by a fit to the experimental cross sections. The transition probability of the system from the ground state to the excited state at a crossing point was tentatively described with the Landau–Zener formula. For the interpretation of this work it appeared to be a serious obstacle that only a few data were known of the potential curves playing a role in the non-violent inelastic scattering of heavy particles. Therefore the potential curves of the excited states were approximated with the help of Koopman's rule, in which the total energy of the system is thought to be built up by the eigenvalues of the electron energies as determined in the field of two shielded nuclei. These eigenvalues, therefore, had to be known as a function of the distance between the nuclei. Lichten[11]) estimated the eigenvalues of the Ne–Ne and the Ar–Ar system in his explanation of the promotion of inner-shell electrons.

At a crossing of a molecular orbital, which contains an inner-shell electron, and an unfilled molecular orbital the electron can be promoted into this empty level which, after separation, corresponds to an outer-shell state.

In the symmetric heavy-collision case the triply peaked structure in the inelastic energy loss is generally explained by the fact that either no electron (peak I), or one inner-shell electron (peak II), or two inner-shell electrons, one in each of the collision partners (peak III), can be promoted.

Rotational coupling which is operative between states with nearly degenerate energies, which differ only by one orbital with a change of magnetic quantum number of ± 1, is another mechanism which might be responsible for transitions to inelastic channels.

McCaroll *et al.*[17]) presented, during the last ICPEAC conference, evidence that inelastic $Li^+ + He$ collision measurements of Lorentz *et al.*[18]) could be explained by this mechanism. In that conference also a paper was presented by a Russian

group[19]) which contained "collision spectroscopy" of the pairs K^+ and Na^+ on Ar and Ne.

The identification of the peaks in the Q spectrum is sometimes hampered because with inelastic-energy loss a process where the ion and the target particle are excited, is nearly identical to a process where the target is excited into an autoionizing state. This problem was already pointed out by Aberth and Lorentz in connection with their He^+–Ar inelastic energy-loss measurements. In the later work of Barat *et al.* the choice was not explicitly made and all inelastic losses were attributed to excitation of the neutral target atom leaving the projectile completely unexcited. Recently, work in the same field was started at energies above 30 keV[20]). In the Ne^+–Ne case a structure was found which deviated considerably from that found in work with lower primary energies, and which could not be attributed to single-electron excitations of the target atom. Therefore the work was extended to the missing-energy range of 3.5–30 keV. This work is presented in this paper together with a more detailed description of the inelastic energy-loss measurements in the higher-energy range.

2. *Apparatus and experimental method.* 2.1. Apparatus. The experimental setup is shown in fig. 1. A 200 keV isotope separator[21]) is used to produce the primary-ion beam in the energy range above 30 keV. Below this energy the ions were extracted from another beam machine called Cesar[22]). 4 keV measurements were performed on a mass spectrometer with a uno-plasmatron source. The ions were subsequently scattered through small angles ($\theta_1 < 2°$) by a single collision and then energy-analyzed. The energy resolution of the analyzer is $< 5 \times 10^{-4}$. A description of the detection system, along with a more detailed discussion of the apparatus, has been given in a paper about oscillations in inelastic energy losses as a function of Z_1[23]).

The beam-defining diaphragms and the analyzer-entrance apertures are optically aligned to within 3′. The setting of the scattering angle is read off a graduated rim with an accuracy of 3′. The collimating diaphragms for the primary beam restrict the angular spread to 5′. For the electrostatic-energy analyzer the acceptance

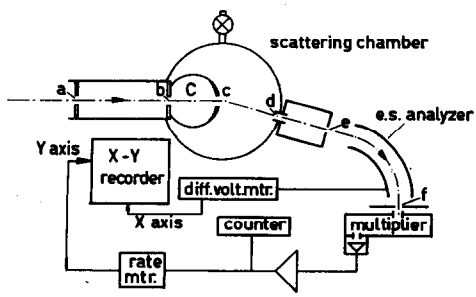

Fig. 1. Schematic view of the experimental setup.

angle is 7.6′. These apertures together cause a distribution in the scattering angles of the observed particles around the scattering angle with a full width at half maximum of 4.6′[23]). The inelastic energy loss is determined by the voltage on the analyzer plates. V_0 is the voltage applied to get the primary beam, V_1 the voltage to get the scattered particles through the analyzer. Then Q is given by

$$\frac{Q}{E_0} = \frac{2}{\alpha}\left(\frac{V_1}{V_0}\right)^{\frac{1}{2}} \cos\theta_1 - \frac{1-\alpha}{\alpha} - \frac{1+\alpha}{\alpha}\left(\frac{V_1}{V_0}\right), \tag{1}$$

with an error $\Delta Q < (13 + 6/\alpha) \times 10^{-5}\, E_0$ for our apparatus.

If in the spectrum the elastic peak is resolved and the voltage on the analyzer plates to get the elastically scattered particles through is V_1 (elastic), the relation to calculate Q can be approximated by

$$Q/E = [V_1 \text{ (elastic)} - V_1 \text{ (inelastic)}]/V_0, \tag{2}$$

with an error $\Delta Q \approx 6 \times 10^{-5}\, E_0$ for our apparatus.

The derivation of (1) and (2) can be found elsewhere[32]).

2.2. The measurement of cross sections. To get the relative differential cross section for the different peaks in the inelastic energy-loss spectrum (see section 4.1) we have measured the intensities of the separate peaks:

$$I = Nn\sigma(\theta_1) \sin\theta_1 \, d\theta_1 \, d\phi, \tag{3}$$

with n the number of scattering centres, N the number of incident ions per second, θ_1 the scattering angle. n is proportional to the target density (ϱ), which has been kept constant during the intensity measurements. Moreover, it is proportional to the volume in the target chamber from which it is possible, after scattering, to enter the analyzer at a given setting of the scattering angle θ_1, as explained in section 1. This "scattering volume" is essentially the intersection of the beam with the cone, which is defined by the analyzer-entrance apertures, and varies with the scattering angle θ_1. It can be approximated by

$$n = \varrho \times \text{volume} \approx \varrho\,(c'/\sin\theta_1) = c/\sin\theta_1 \qquad (c' \text{ constant}).$$

So

$$I = N\,(c/\sin\theta_1)\,\sigma(\theta_1) \sin\theta_1 \, d\theta_1 \, d\phi = \text{constant}\,\sigma(\theta_1).$$

However, for very small scattering angles ($\theta_1 < 55'$) the scattering volume is cut off by a diaphragm and an analyzer-entrance aperture, because of the dimensions of the scattering chamber. This decrease of the scattering volume is a function of the scattering angle and introduces a correction factor $f(\theta_1)$. The resulting expression for the intensity I is:

$$I = \text{constant}\, f(\theta_1)\, \sigma(\theta_1). \tag{4}$$

3. Ar^+–Ar *collisions.* 3.1. General. Measurements were performed with the following energies for the primary Ar^+ ions: 7.5 keV, 10 keV, 15 keV, 25 keV, 30 keV, 40 keV and 60 keV. Typical scattering angles were in the range between 10 and 90 minutes of arc. The collision is characterized by the quantity $\tau = E_0\theta$, where E_0 is the impact energy and θ the scattering angle in the laboratory system.

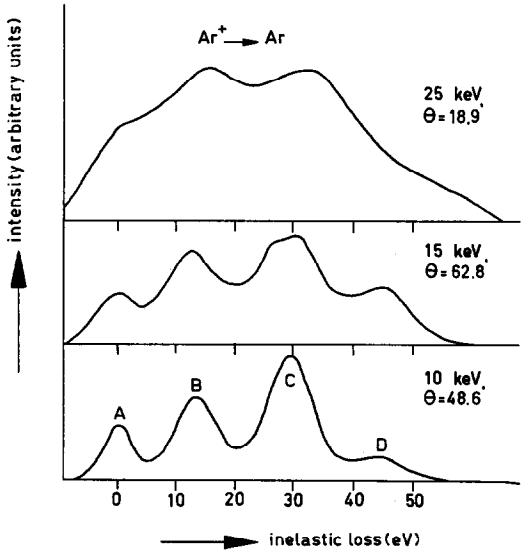

Fig. 2. Energy-loss spectra arising from scattering of Ar^+ by Ar at three different primary energies. Scattering angles in the lab. system are: a) at 10 keV, 48.6 min; b) at 15 keV, 62.8 min; c) at 25 keV, 18.9 min.

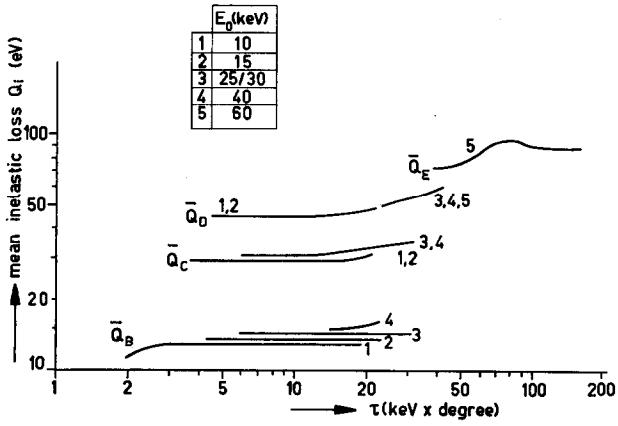

Fig. 3. Mean inelastic energy losses of the different peaks in the Ar^+–Ar energy-loss spectra as a function of τ. Note that for 60 keV a new peak E occurs in the spectrum.

In small-angle forward scattering this quantity is primarily a function of the impact parameter p[24]). The relationship between τ and p is determined by the interaction potential. One has to bear this in mind while comparing two peaks containing particles which have followed different potential surfaces at the same τ. This problem will be discussed in detail in section 5.

In figs. 2a, 2b and 2c examples of secondary-energy spectra are given, respectively for impact energies of 10, 15 and 25 keV. For physical as well as non-physical reasons (see section 3.3) the structure in the spectra becomes less pronounced towards higher primary energies. This inhibits the identification of the collision process at these energies.

3.2. Identifications of the collision process. In general, four peaks can be resolved: the elastic peak A and three inelastic peaks B, C and D. The elastic peak is used as the zero point of the inelastic energy scale. In table I a summary concerning the data of the different peaks is given for 10 and 15 keV. Further details are given in fig. 3.

TABLE I

Mean inelastic-energy losses and observed width of the different peaks in the spectrum

Peak	$E_0 = 10$ keV		$E_0 = 15$ keV	
	$\bar{Q}$ (eV)	$\overline{\text{FWHM}}$ (eV)	$\bar{Q}$ (eV)	$\overline{\text{FWHM}}$ (eV)
A	0	6.7	0	9.0
B	12.2	8.2	13.4	10.0
C	29.5	9.6	29.5	13.0
D	45.5	10.5	45.6	11.9

3.2.1. Peak B. This peak, which is also measured in the lower-energy range can be attributed to two processes.

B1: $Ar^+ + Ar(3p^6) \rightarrow Ar^+ + Ar^*(3p^5, nl)$,

excitation of the 3p electron in the target particle to an excited state, for instance:

to $Ar^*(3p^5, 4s)$ with $Q = 11.5$ eV,

to $Ar^*(3p^5, 4p)$ with $Q = 12.9$ eV, *etc.*

B2: $Ar^+(3s^2, 3p^5) + Ar \rightarrow Ar^{+*}(3s, 3p^6)^2 S_{\frac{1}{2}} + Ar$,

excitation of the 3s electron in the projectile with $Q = 13.5$ eV.

3.2.2. Peak C. One has to bear in mind that the inelastic-energy loss Q is essentially connected to a collision process and not to a specific particle. Therefore several processes might explain the occurrence of the second inelastic peak.

$$\text{C1:}\quad Ar^{+} + Ar\,(3s^2, 3p^6) \rightarrow Ar^{+} + Ar^{**}\,(3s^2, 3p^4, n_1l_1, n_2l_2)$$
$$\rightarrow Ar^{+} + Ar^{*}\,(3s, 3p^6, n_1l_1),$$

the excitation by a one- or two-electron promotion to an auto-ionizing state of the target particle, for instance to

$Ar^{**}\,(3s^2, 3p^4, 4s, 4p)$ with $Q = 29$ eV or

$Ar^{*}\,(3s, 3p^6, 4s)$ with $Q = 25.8$ eV, *etc.*

$$\text{C2:}\quad Ar^{+}\,(3s^2, 3p^5) + Ar\,(3s^2, 3p^6)$$
$$\rightarrow Ar^{+*}\,(3s^2, 3p^4, nl) + Ar^{*}\,(3s^2, 3p^5, nl)$$
$$\rightarrow Ar^{+*}\,(3s, 3p^6) + Ar^{*}\,(3s^2, 3p^5, nl),$$

the simultaneous excitation of the target and the projectile, for instance

$Ar^{+*}\,(3s^2, 3p^4, 3d) + Ar^{*}\,(3s^2, 3p^5, 4s)$ with $Q = 28$ eV or

$Ar^{+*}\,(3s, 3p^6) + Ar^{*}\,(3s^2, 3p^5, 4p)$ with $Q = 26.4$ eV, *etc.*

3.2.3. Peak D. Again some processes are possible:

$$\text{D1:}\quad Ar^{+} + Ar\,(3s^2, 3p^6) \rightarrow Ar^{+} + Ar^{**}\,(3s, 3p^5, n_1l_1, n_2l_2),$$

excitation of an auto-ionizing state of the target atom in which a 3s and a 3p electron are promoted, for instance to

$Ar^{**}\,(3s, 3p^5, 3d, 4s)$ with $Q = 44.7$ eV, *etc.*

$$\text{D2:}\quad Ar^{+}\,(3s^2, 3p^5) + Ar\,(3s^2, 3p^6)$$
$$\rightarrow Ar^{+*}\,(3s^2, 3p^4, nl) + Ar^{**}\,(3s^2, 3p^4, n_1l_1, n_2l_2);$$

the simultaneous excitation of the target and the projectile, the former to an auto-ionizing state, the latter to an excited state. Examples are:

$Ar^{+*}\,(3s^2, 3p^4, 3d) + Ar^{**}\,(3s^2, 3p^4, 4s, 4p)$ with $Q = 45.5$ eV or

$Ar^{+*}\,(3s, 3p^6) + Ar^{**}\,(3s^2, 3p^4, 4s, 4p)$ with $Q = 42.5$ eV, *etc.*

A definite choise among all these possible collision processes is difficult to make. It is quite possible that sometimes different excitation channels contribute to one peak.

3.3. Widths. The full width at half maximum of the elastic peak is caused by the finite resolution of the energy analyzer ($\Delta E/E_0 \approx 5 \times 10^{-4}$) and the spread in the primary-beam energy of *ca.* 4 eV. The contribution due to thermal motion of the target atoms can be neglected.

The widths of the inelastic peaks are caused by the same effects and by the natural width of the peaks. That is, by the distribution of excitation channels contributing to the inelastic peak. By deconvolution of the inelastic peak with the elastic one we have found the natural widths as given in table II.

TABLE II

Peak widths caused by physical effects		
	Natural peak widths	
Peak	at 10 keV	at 15 keV
B	4.8 eV	4.4 eV
C	7.0 eV	9.4 eV
D	7.7 eV	7.7 eV

3.3.1. Discussions of the widths of peaks B and D. The width of the first inelastic peak (4.6 eV) corresponds well to the range of accessible excitation channels assuming that process B1 is responsible for peak B (4.2 eV). Thus we assume that in any case collisions of the type B1 contribute to peak B, although this observation does not exclude collision processes of the type B2.

The width of peak D gives no further indication with regard to identification of the collision process.

Also some vague correlations in the cross sections of the different peaks (see section 3.6) are not very helpful because it is not known whether one can construct the probability for simultaneous excitation of target and projectile from the probabilities of both processes alone or that both processes are interdependent. For instance it could be that excitation of the ion can *only* take place if the target is excited also. Note that a peak around 18 eV indicating excitation of the Ar^+ projectiles *alone* has never been observed.

3.3.2. Anomalous broadening of peak C. From table II it is seen that the width of peak C at 15 keV impact energy is much larger than at 10 keV while the natural widths of the other two inelastic peaks are independent of the primary

energy within the experimental error. The reason for this broadening is found by a closer examination of peak C in fig. 2b. The peak is composed of two unresolved peaks at about 26 eV and 30 eV. Evidently the 26 eV component is, for 10 keV impact energy but at the same τ value, not visible. This phenomenon is contrary to the general trend in the inelastic energy-loss measurements: with increasing primary energy and scattering angle the most probable transition shifts towards transitions with a higher energy deficit. It might be that the transition responsible for the 26 eV component in peak C is due to rotational coupling since the probability for such a transition is always increasing with increasing energy.

3.4. Coincidence measurements. Measurements of Kessel *et al.*[3]) for the Ar^+–Ar system have shown Q values of about 28.5 eV occurring during the processes $Ar^+ + Ar \rightarrow Ar^+ + Ar - Q$ (1010), in which no ionization takes place. This means that no auto-ionizing state is formed in this collision which de-excites *via* electron ejection. Our peak C has a mean Q value of 29.5 eV and it is therefore natural to connect it with this measurement of Kessel. So this peak must be explained by processes of type C2, for C1 leads to processes like $Ar^+ + Ar \rightarrow Ar^+ + Ar^+ - Q$ (1011). The anomalous broadening can be due to a 3s promotion followed by de-excitation through light emission.

In the same experiment processes (1011) led to inelastic losses between 55 and 62 eV. These values are somewhat too high to connect them with our peak D (45.5 eV). However, the τ values in Kessel's experiment were much higher, which may have led to the opening of the higher members of the families of excitation processes D1 and D2. The upper limits of both processes are 58.2 and 61 eV, respectively. So only process D2 can cover the highest Q value measured by Kessel in the process (1011).

Summarizing we come to the following thesis.

1) Peak B is mostly due to collision processes in which excitation of a 3p electron in the target particle takes place (B1).

2) In peak C particles arising from processes in which simultaneously the 3p electrons in the ion and the atom are excited, are preponderant (C2). (The extra structure at 15 keV, $\theta_1 \geqslant 1°$ can tentatively be ascribed to a 3s-electron promotion in the target atom.)

3) Peak D may be due to collision processes in which the ion is excited and the target atom is excited to an auto-ionizing state (D2).

3.5. The shell model of inelastic-energy loss. It was found in the heavy-collision range ($\tau > 100$ keV deg) that the mean inelastic-energy loss, defined as

$$\bar{Q} = \int P(Q)\, Q \, \mathrm{d}Q, \tag{5}$$

did rise rapidly in specific regions of distance of closest approach. These regions have been correlated to distances at which different (sub)shells geometrically

overlap. The electron–electron interaction in overlapping shells becomes very strong causing a rapid change in the energies of the molecular orbitals. This can result in several potential curve crossings in that particular region.

In fig. 4 the $\bar{Q}$ values taken at different E_0 are plotted as a function of τ as far as the present measurements are concerned. They are compared with the measurements of refs. 1, 3, 6 and 9 where $\bar{Q}$ is plotted against r_0. The measurements are in good agreement.

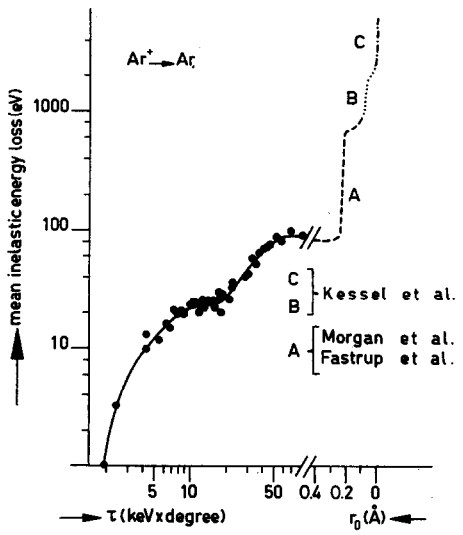

Fig. 4. Mean inelastic-energy losses as a function of the violence of the collision, τ, compared with measurements of other authors in the more violent collision range ($r_0 < 0.4$ Å)[1,3,6,9].

Tentatively one can attribute the rapid change in $\bar{Q}$ from 0 to 22 eV ($2 < \tau < 10$ keV deg) to interaction between the two M II subshells (appearance of peaks B and C). The rise from 30 to 90 eV ($20 < \tau < 50$ keV deg) may be correlated to the interaction of the M II subshell of the target atom with the M I subshell of the Ar^+ ion (appearance of peak D).

These considerations are rather superficial as they do not explicitly state which transitions exactly are involved. However, the fact is emphasized that the inelastic-energy loss is due to excitation families which have well-defined upper limits. This is in strong contrast with the case of Ne^+ scattering on Ne where the $\bar{Q}$–τ plot does not allow this conclusion (see 4.3).

3.6. Cross sections for Ar^+–Ar collisions. 3.6.1. Elastic differential cross sections. In fig. 5 the relative differential cross sections of the elastically scattered particles, calculated from the intensity, using eq. (4), have been plotted against θ_1 for three different primary energies. No absolute cross sections could

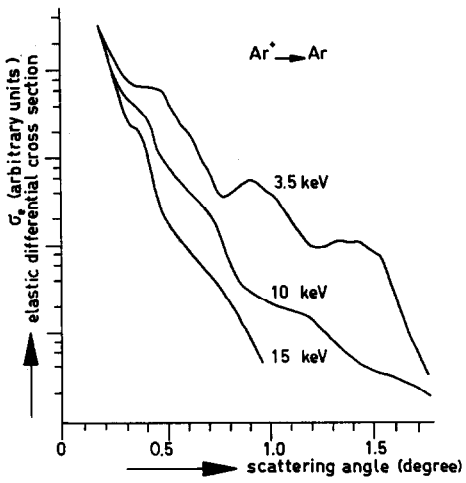

Fig. 5. Elastic differential cross sections for Ar^+–Ar scattering. The curves for three different primary energies are normalized at a scattering angle of 12 min.

be obtained because absolute beam-current measurements were prohibited at very small angle scattering due to geometrical reasons. In table III the maxima and minima which are observed are tabulated.

Comparison of our data with data of ref. 16 shows the same trend: a shift of the extrema towards lower values for higher primary energies as is theoretically predicted. The results at 3 keV in this reference and our results at 3.5 keV do fit quite well. Furthermore a new maximum is discovered in the very low scattering-angle region.

The amplitude of the oscillations in the elastic cross sections, which are caused by interference of partial waves scattered by the ungerade and gerade potentials diminish with higher primary energies. Different reasons for the damping towards

TABLE III

	Scattering angles at which extrema in σ_e are observed					
E_0 (keV)	Min_1	Max_1	Min_2	Max_2	Min_3	Max_3
15	0.25	0.35	0.50	–	–	–
10	0.28	0.38	0.48	0.71	0.89	1.16
3.5	0.33	0.48	0.77	0.92	1.22	1.43
3[a]	–	–	0.81	1.03	1.25	–

[a] Taken from ref. 16.

larger energies can be considered. First of all the finite angular resolution causes the width of the impact-parameter region which is studied at a given scattering angle to increase with primary energy. Complete annihilation can only be attained if two waves are scattered over the same angle along different orbits in such a way that the phase shifts after the collision differ exactly by $(2N + 1)\,\pi$ and each of the waves has the same amplitude. To observe such an effect an infinitely small angular resolution is required. As this is not the case the observed cross sections are in fact experimentally integrated over a range of impact parameters and thus over a range of phase shifts which causes a damping. The integration interval increases approximately linearly with the primary energy.

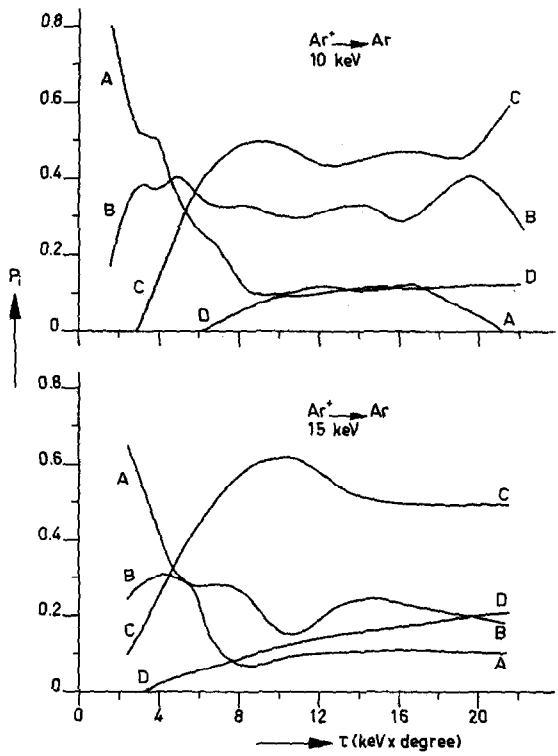

Fig. 6. Relative peak areas of the different peaks in the Ar–Ar energy-loss spectrum as a function of τ. A: elastic peak; B: $\bar{Q} = 13$ eV; C: $\bar{Q} = 29.5$ eV; D: $\bar{Q} = 45.5$ eV.

Secondly it can be seen in fig. 6 that at higher energies the majority of the projectiles have been scattered inelastically. The loss of particles into the inelastic channels affects the two components leading to elastic scattering (the gerade and ungerade partial waves) in different ways.

3.6.2. Inelastic differential cross sections. Fig. 7 shows an example of the relative differential cross sections of the inelastic peaks at 10 keV. From this figure a plot of relative excitation probabilities can be constructed. This is done for 10 and 15 keV in fig. 6, where the relative peak areas are plotted against τ.

1) The elastic peak A has nearly the same relative probability in the 10 keV and 15 keV cases.

2) The first inelastic peak B has a rather oscillating behaviour. Note the large maximum at $\tau = 20$ for 10 keV and the pronounced minimum at $\tau = 11$ for 15 keV bombardment.

3) The second inelastic peak C has a broad maximum at $\tau = 10$ especially for $E_0 = 15$ keV. It may be connected with the occurrence of the anomalous broadening of this peak in this region. Then it is also possible to explain the dip

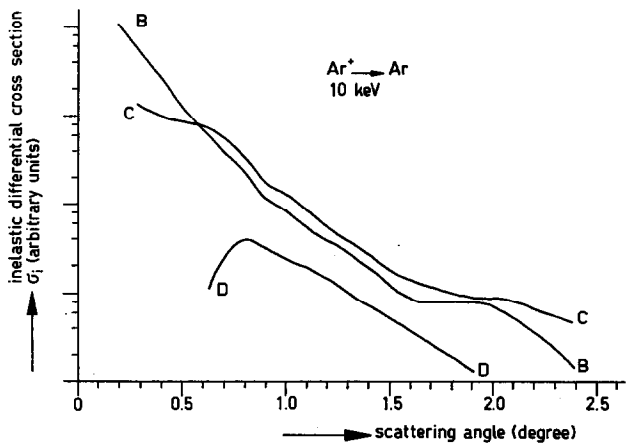

Fig. 7. Inelastic differential cross sections for the different peaks in the 10 keV Ar^+–Ar energy-loss spectrum. B: peak with $\overline{Q} = 13$ eV; C: peak with $\overline{Q} = 29.5$ eV; *D*: peak with $\overline{Q} = 45.5$ eV.

in peak B at around the same τ. Evidently if the target particles are excited to auto-ionizing states ($3s, 3p^6, nl$; $Q = 26$ eV → maximum peak C) they are no longer observed as p-electron excited atoms ($3s^2, 3p^5, nl$; $Q = 13$ eV → minimum in peak B).

4. Ne^+–Ne *collisions.* 4.1. Identification of the collision process. Measurements were performed with the following energies of the primary Ne^+ ions: 3.5 keV, 4 keV, 5 keV, 8 keV, 10 keV, 15 keV, 20 keV, 25 keV, 30 keV, 60 keV and 90 keV. Typical scattering angles were in the range between 10 and 90 min. In figs. 8a, 8b and 8c examples of the secondary-energy spectra are given for impact energies of 8, 20 and 30 keV.

In general three large peaks are observed: the elastic one A, and two inelastic ones B and C. For the lower primary energies B and C have their maxima at ± 20 and ± 55 eV, respectively. However, at 30 keV the first inelastic peak has its maximum at ± 28 eV and the second one at ± 67 eV. Both inelastic peaks seem to have shifted towards higher energy losses. This shifting of peak B is continued until B reaches values of the order of 45 eV and its magnitude has been decreased

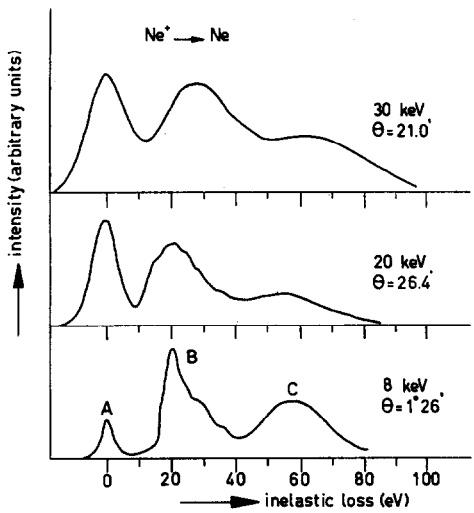

Fig. 8. Energy-loss spectra arising from scattering of Ne^+ by Ne at three different primary energies. The scattering angles are given in the lab. system.

such that it can no longer be observed. The difference in inelastic-energy loss between the two inelastic peaks increases from 36 to 55 eV. This behaviour of the peaks as a function of τ makes it very difficult to identify the collision processes leading to these characteristic inelastic-energy losses. For instance peak B can be explained in the range where $\tau < 10$ keV deg and $E_0 < 10$ keV by an excitation of a 2p electron in the neon target:

$$Ne^+ + Ne(2p^6) \rightarrow Ne^+ + Ne^*(2p^5, nl),$$

for instance $Ne^*(2p^5, 4s)$ with $Q = 19.6$ eV.

A closer examination of peak B in this range shows that it is asymmetric with a tail lying in the first continuum. It reveals also some structure in the peak itself. Therefore we performed a higher-resolution measurement at a primary energy of 4 keV. (The energy spread in the primary beam was reduced to 1.7 eV.) A typical result is shown in fig. 9. One observes that peak B has two components in the continuum, the first lying at ± 23.4 eV; the second one at ± 27 eV. It is impossible

to explain the 23.4 eV peak in terms of spectroscopically known levels. It must be emphasized that this small peak is systematically observed during the measurement on two different apparatuses used in our experiments. The 27 eV component could be explained by the processes:

$$Ne^+ + Ne \rightarrow Ne^{+*}(2s, 2p^6) + Ne - 28.6\,eV$$

and

$$Ne^+ + Ne \rightarrow Ne^{+*}(2p^4, 3s) + Ne - 27.1\,eV,$$

with single excitation of the projectile.

At larger scattering angles also small discontinuities are observed at ± 31 and ± 35 eV. The shifting of peak B might then be explained by the subsequent increase of the mentioned components, with increasing τ. Another interesting feature in peak B is that in our work the lowest possible excitation

$$Ne^+ + Ne \rightarrow Ne^+ + Ne^*(2p^5, 3s) \quad \text{with} \quad Q = 16.7\,eV,$$

is observed as an unresolved hump at the lower inelastic energy-loss side of peak B in contrast to the observations in the work of Barat *et al.*[16]).

The maximum of the second inelastic peak C shifts from 51 eV at 4 keV primary energy to 67 eV at 30 keV. It can partly be attributed to auto-ionization of

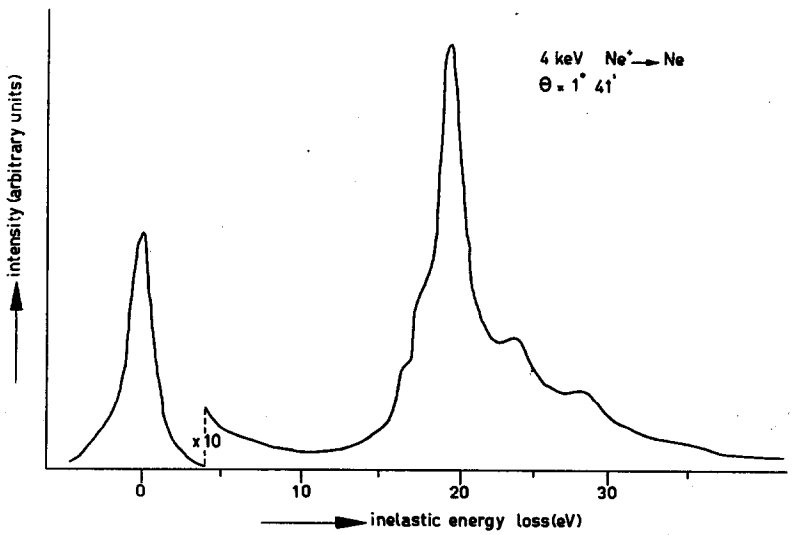

Fig. 9. Large resolution measurement of the ± 20 eV inelastic energy-loss peak in the Ne^+–Ne energy-loss spectrum.

the target atom:

$$Ne^+ + Ne \rightarrow Ne^+ + Ne^{**}(2p^4, n_1l_1, n_2l_2)$$

for instance $Ne^{**}(2p^4, 3p, 4p)$ with $Q = 51.6$ eV.

But the highest inelastic-energy losses observed in this peak cannot be explained by this process as double ionization needs only 62 eV.

4.2. Coincidence measurements and theoretical calculations. As was the case for Ar^+–Ar collisions, coincidence measurements[4]) can partly elucidate the problem of which collision processes cause the observed inelastic-energy losses in our spectra. We have also used some calculations of Thulstrup and Johansen[22]) on pseudomolecular states of the (Ne–Ne^+) molecule for different internuclear distances, to solve the identification difficulties.

The lowest $\bar{Q}$ value in the tables of ref. 4 is 45 ± 20 eV corresponding to a (1010) process ($\tau = 64$ keV deg). It follows that although processes occur with inelastic-energy losses larger than the first ionization potential, ionization does not occur. This may be explained by simultaneous excitation of target atom and projectile; the alternative explanation of excitation to an auto-ionizing state followed by emission of a photon seems improbable. In our measurements the shifting of peak B from an inelastic energy loss of ± 20 eV at $\tau = \pm 5$ keV deg to an inelastic energy loss of ± 50 eV at $\tau = \pm 50$ keV deg can therefore be explained by a gradual change from excitation of target atom to excitation of both projectile and target atom. This leaves, however, an unexplained τ region about 10 keV deg where $21.6 < \bar{Q} < 26.8$ eV.

Thulstrup and Johansen have an alternative explanation for the shifting of peak B. They show that the pseudomolecular (Ne–Ne^+) states penetrate the (Ne–Ne^+) ionization continuum. The shifting is then explained as a gradual change from excitation of the target atom to direct ionization of this atom. However, if this occurs, the $\bar{Q}$ values of about 25 eV would correspond to (1011) processes. This is in contradiction with the value of $\bar{Q} = 70 \pm 5$ eV which is found by Kessel *et al.* for the (1011) process ($\tau = 64$ keV deg).

It seems that this last observation of Kessel is related to the second inelastic peak C which in our measurements has $\bar{Q}$ values in the range 50–200 eV. $\bar{Q}$ values of ± 70 eV would be obtained by simultaneous excitation of the projectile and auto-ionization of the target atom. If the last one should de-excite by electron ejection, the collision process would indeed be of the type (1011). An alternative explanation of the second peak is also given by Thulstrup and Johansen:

$$Ne^+(2p^5) + Ne(2p^6) \rightarrow Ne^+(2p^5) + Ne^{++}(2p^4) + 2e,$$

with direct double ionization which becomes possible if the (Ne–Ne^+) ground state penetrates the second ionization continuum of the (Ne–Ne^+) pseudomole-

cule. This fits better with the coincidence work and the experiment because $\bar{Q}(1012) = 100 \pm 10$ eV and the peak C has exactly that value for 64 keV deg. It must be remarked that the (1012) process is the most important one in this τ region. These processes can lead to an inelastic-energy loss of at most ± 160 eV. Therefore the 90 keV results must be due to (1013) processes.

4.3. Mean inelastic-energy loss as a function of the violence of the Ne^+–Ne collision. As we observe three peaks A, B and C in the energy-loss spectrum the mean inelastic-energy loss $\bar{Q}$ is defined as:

$$\bar{Q} = P_A\bar{Q}_A + P_B\bar{Q}_B + P_C\bar{Q}_C, \tag{6}$$

in which P_A, P_B and P_C are the probabilities for excitation of the peaks A, B and C. $\bar{Q}_A = 0$ eV, $\bar{Q}_B$ and $\bar{Q}_C$ are the average energy losses in peaks B and C, respectively.

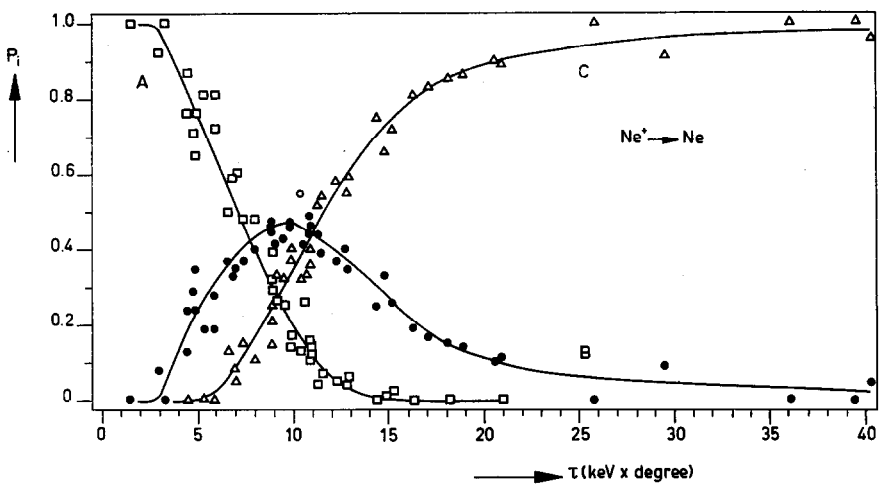

Fig. 10. Probabilities for excitation of the different peaks in the Ne^+–Ne energy-loss spectrum. All the measurements, taken at energies from 3.5 keV to 90 keV are collected in this figure. A: elastic peak; B: inelastic peak, $\bar{Q}$ varies from ± 18 to 50 eV; C: inelastic peak, $\bar{Q}$ varies from ± 50 to 250 eV.

Fig. 10 shows a plot of P_A, P_B and P_C against τ for different primary energies. Within the accuracy of the measurement these functions are independent of the primary energy.

Fig. 11 shows $\bar{Q}_B$ and $\bar{Q}_C$ as functions of τ for different primary energies. From figs. 10 and 11 we have constructed with the help of eq. (6) the $\bar{Q}$–τ dependence in fig. 12. This is averaged over the different primary energies.

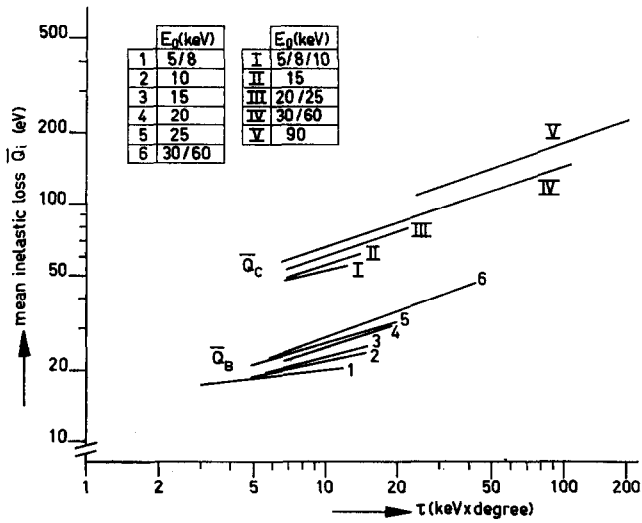

Fig. 11. Mean inelastic-energy losses of the different peaks in the Ne^+–Ne energy-loss spectra for different energies as a function of τ.

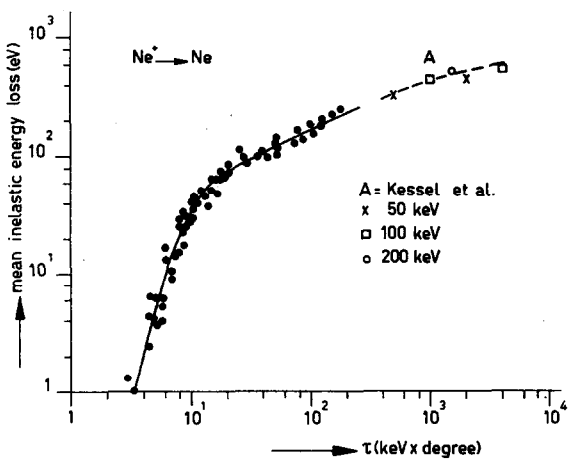

Fig. 12. Mean inelastic-energy loss of Ne^+ ions scattered by Ne atoms as a function of τ.

For τ values up to ± 15 keV deg it can be seen that the $\bar{Q}$ values increase rapidly. Then the increase is slower but these values never reach a plateau as in the Ar^+–Ar case. The reason for this can easily be found in the figs. 10 and 11. The only quantities in eq. (6) which keep rising even above 20 keV are the $\bar{Q}_B$ and $\bar{Q}_C$ values, the shifting of the inelastic peaks. Due to this shifting a qualitative consideration of the Q–τ plot in terms of overlapping shells is not possible. Our

highest $\bar{Q}$ values obtained for primary energies of 60 and 90 keV fit rather well to the values of Kessel *et al.*[4]) taken at energies of 50 and 100 keV.

5. *Calculations.* 5.1. Critical internuclear distances for potential curve crossing. From fig. 10 it can be seen that for $Ne^+ + Ne \rightarrow Ne^+ + Ne^*$ (peak B) the threshold is at about 2.3 keV degree. Assuming that the excited particles of peak B are promoted *via* the outermost r_c, from the orbital energies as given by Lichten[11]) and calculated by Thulstrup and Johansen[22]) it can easily be seen that the first crossing is the one between the Σ_g (Ne^+–Ne) ground state and the Σ_g [$Ne^+(2p^5)$–$Ne^*(2p^5, 3s)$] excited state. This transition in which parity and magnetic quantum number are conserved cannot be due to rotational coupling. Therefore the transition probability can be given by the well-known Landau–Zener formula[26]):

$$P = \exp\left[-u/v_{\mathrm{rad}}(r_c)\right], \tag{7a}$$

where $v_{\mathrm{rad}}(r_c)$ is the radial velocity at an internuclear distance of r_c and

$$u = \frac{2\pi}{\hbar} H_{12}^2 \Big/ \left| \frac{\partial}{\partial r} (H_{11} - H_{22}) \right|_{r=r_c} . \tag{7b}$$

H_{12} which is not velocity dependent is half the energy between the adiabatic potential curves at the pseudo-crossing and

$$\frac{\partial}{\partial r} |(H_{11} - H_{22})|_{r=r_c} \tag{7c}$$

is the difference in slope of the potential curves at $r = r_c$.

The particles pass through the crossing point twice, therefore the fraction of particles separating in the excited state is $2P(1 - P)$.

The differential-excitation cross section $\sigma(\theta)$ will therefore show a threshold behaviour which is governed by the Landau–Zener relation and more specifically by $v_{\mathrm{rad}}(r_c)$. Evidently if $r_0 = r_c$ and $v_{\mathrm{rad}}(r_c) = 0$ the cross section is zero. Extrapolation of the differential cross section to zero therefore should give the θ for which $v_{\mathrm{rad}}(r_c) = 0$ and, if one knows the potentials, it is possible to calculate from this θ the critical internuclear distance. (Note that this is a circular problem: if one knows the potentials one knows also their crossing point.)

However, it will turn out to be not as simple as sketched above due to a peculiarity in the calculated θ–p plot. The minimum θ value occurring in that function is not obtained *via* the orbit which has $r_0 = r_c$. This complication is taken into account.

Thulstrup did *ab initio* calculations of the Σ_g ground-state potential with respect to the Ne_2 potential as a function of r. We used for the ground state of the Ne_2

system an exponential potential[27]) which is known to be a good approximation around 1 Å. The Σ_g (Ne^+–Ne) ground potential can then be fitted to the calculations of Thulstrup.

$$V_{\Sigma_g(Ne^+-Ne)}(r) = V_{(Ne-Ne)}(r) + 21 + 222\exp(-2.88\,r), \tag{8}$$

with $V_{(Ne-Ne)}(r) = 8200\exp(-4.57\,r)$ and $0.5 < r < 3$ Å (fig. 13). This potential should describe collisions in this region better than the potential calculated by Lane and Everhart from their cross sections. Their potential is known to be too flat in this range.

An approximation of the Σ_g (Ne^+–Ne*) potential is much more difficult to make. These excited-state potentials are generally calculated with the use of Koopman's theorem which states that the total potential energy is the sum of the orbital energies of the different electrons without taking electron–electron interaction into account.

The theorem therefore yields potential curves which are essentially wrong. For instance it is not possible to discriminate between the potential energies of the Ne^{+*} ($2p^4$, 3s)–Ne($2p^6$) and the Ne^+($2p^5$)–Ne* ($2p^5$, 3s) systems as in both cases two 2p electrons are removed and one 3s electron is added. However, from a close

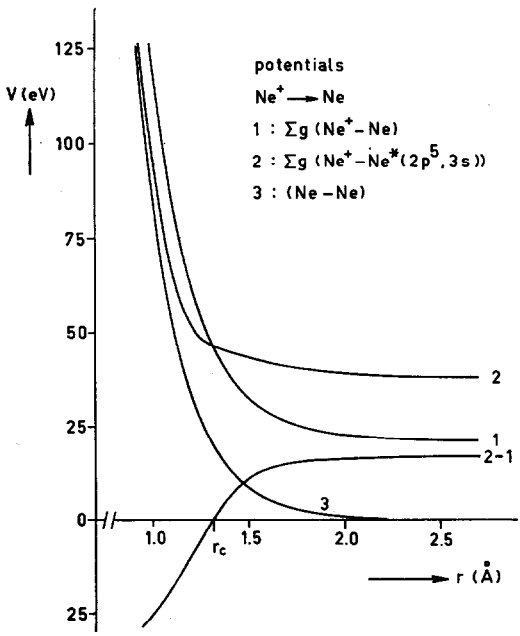

Fig. 13. Potentials describing the process $Ne^+ + Ne \rightarrow Ne^+ + Ne^*$ ($2p^5$,3s). The particles approach *via* the ground-state potential (1) and leave each other *via* the excited-state potential (2). R_c is determined by the cross-section threshold of 2.3 keV deg.

examination of the series of excited-state potentials derived with the help of Koopman's theorem we observe that the potential might be empirically approximated by the following functional form:

$$V_{\Sigma_g[Ne^+-Ne^*(2p^5,\,3s)]} - V_{(Ne-Ne)}(r) = 5 + 16.5\,\{1 + \tanh\,[4.4\,(r - r^*)]\}, \quad (9)$$

for $0.5 < r < \infty$ Å. The constants in this expression are obtained by using its known behaviour at ∞ and at close distances. The factor 4.4 is determined from the slope of the energy-difference curve in the region of high rate of change of this difference. r^* is the separation at which the energy difference between Ne_2 and Ne_2^{+*} is 21.5 eV. By varying this quantity we vary the crossing point of the ground-state Ne_2^+ potential and the excited-state potential.

When we obtained our two potential curves (fig. 13) with an adjustable internuclear distance of curve crossing, we performed a series of orbital calculations for different impact parameters and different r_c (fig. 14).

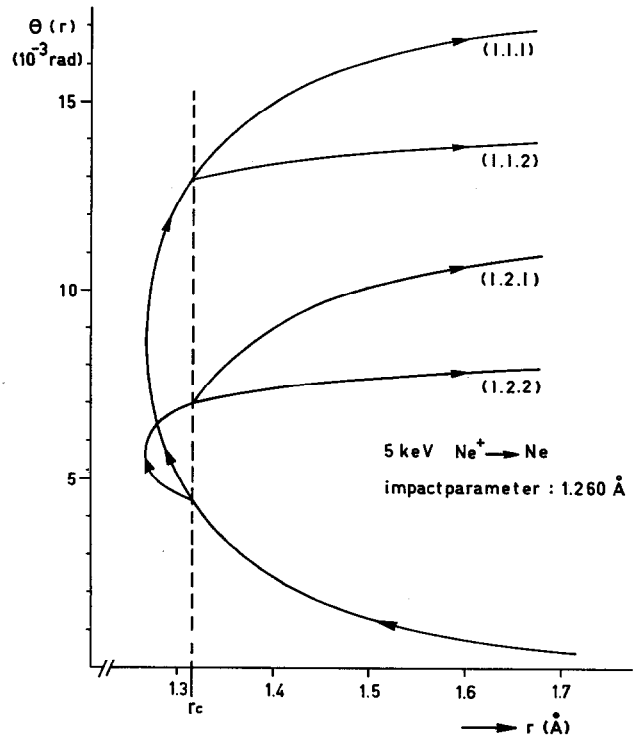

Fig. 14. Example of an orbital calculation for an impact parameter of 1.26 Å. The particles can follow 4 different potential surfaces indicated by the numbers between parentheses. (1.2.1) means that for r-values from ∞ to r_c the potential followed by the particles is 1. From r_c *via* r_0 to r_c the potential between the particles is 2 and from r_c to ∞ the potential is again 1.

An r_c value of 1.32 Å leads to the best fit to experiment because particles which have followed the potential surface leading to the excited state will only be observed for $\tau > 2.3$ keV deg (fig. 15). It can be observed from the same figure that if one does not take the fact of different incoming and outgoing potential curves into account and only uses a ground-state potential (orbit 111), the r_c value, corresponding to 2.3 keV deg, will be 1.47 Å.

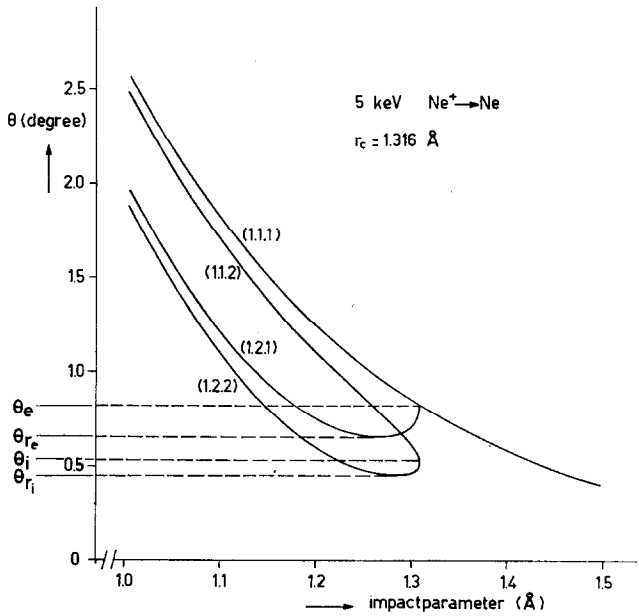

Fig. 15. The relation between impact parameter and scattering angle obtained by orbital calculations. Two potentials are used. This leads to 4 different scattering angles for one impact parameter if $p < 1.32$ Å. Excited particles can only be observed for $\theta > 0.46$ deg or $\tau > 2.3$ keV deg.

5.2. Elastic differential cross section. In fig. 5 it can be seen that the elastic differential cross section for scattering of Ar^+ on argon shows an oscillatory behaviour. These oscillations are due to the interference of the partial waves scattered along the different ground-state potential surfaces, *i.e.*, the gerade and ungerade potentials. $f(\theta)$, the scattering amplitude, determines the scattering cross section

$$\sigma(\theta) = |f_u(\theta) + f_g(\theta)|^2, \tag{10}$$

where f_u and f_g are complex expressions in θ which in general will have different phase factors.

In our case, applying semiclassical calculations using the stationary-phase method with JWKB phase shifts, the scattering amplitude is given by[28]):

$$f_j(\theta) = \frac{1}{k}\left[\frac{L_j}{2\,(-\eta''_{L_j}\sin\theta)}\right]^{\frac{1}{2}} \exp\left[\mathrm{i}\,(2\eta_{L_j} - L_j\theta - \tfrac{1}{2}\pi)\right] \qquad j = \mathrm{g, u}. \tag{11}$$

If we substitute expression (11) in eq. (10), we get the final expression for the differential cross section:

$$\sigma(\dot{\theta}) = \frac{1}{k^2\sin\theta}\left[\frac{L_g}{(\mathrm{d}\theta/\mathrm{d}l)_{L_g}} + \frac{L_u}{(\mathrm{d}\theta/\mathrm{d}l)_{L_u}}\right] + \frac{1}{k^2\sin\theta}\left[\frac{L_g L_u}{(\mathrm{d}\theta/\mathrm{d}l)_{L_g}(\mathrm{d}\theta/\mathrm{d}l)_{L_u}}\right]^{\frac{1}{2}} \cos\left[2\,(\eta_{L_g} - \eta_{L_u}) - \theta\,(L_g - L_u)\right]. \tag{12}$$

To determine the cross section we have to calculate the development of the phase along both potential surfaces. This can be done with various degrees of refinement[29]). To calculate the terms $\eta_{L_g} - \eta_{L_u}$ and $L_g - L_u$ we used the most refined method, where $r_{0_{g,u}} = b/[1 - V_{g,u}(r_0)/E]^{\frac{1}{2}}$ and $v(r) = v(\infty)\,[1 - (b^2/r^2) - V_{g,u}(r)/E]^{\frac{1}{2}}$.

However, in the case of Ar^+ on Ar the situation is more complicated, because the magnetic quantum number $m = 0$ or $m = \pm 1$ leads to four molecular states: Σ_u, Σ_g, Π_g, Π_u. This means that there are four ground-state potential curves involved in elastic scattering. The Π and Σ states both contribute an oscillating term to the elastic differential cross section. Since only one oscillation frequency was observed and the frequency of oscillation is related to the energy difference between the gerade and ungerade potential curves, we could deduce that the oscillation frequency in the cross section due to Σ-state interference is considerably higher than the one due to Π-state interference. So high, in fact, that it could not be observed with our angular resolution. This conclusion is justified[30]) by the fact that even over a large scattering-angle interval only one kind of oscillation is observed.

By fitting the calculations to the experimental results it is possible, in principle, to deduce the potentials V_{Π_g} and V_{Π_u}. We tried several Π_g and Π_u potentials and found the pattern of maxima and minima extremely sensitive to them. A Bohr potential and a ΔE function taken from Barat *et al.*[16]) and Jones *et al.*[30]),

$$\begin{aligned} V_{\Pi_g} &= (3200/r)\exp(-r/0.215) - \tfrac{1}{2}\Delta E \quad (\text{in eV}), \\ V_{\Pi_u} &= V_{\Pi_g} + \Delta E, \quad \Delta E = 490\exp(-r/0.29) \qquad (\text{in eV}), \end{aligned} \tag{13}$$

gave a reasonable fit to our results (see table IV).

This reasonable fit was to be expected since the extrema in the cross section measured by these groups closely resemble those found in the present experiment.

TABLE IV

Scattering angles in degrees at which extrema in σ_e are observed for three primary energies, by experiment and calculation

	3.5 keV		10 keV		15 keV	
	θ exp.	θ calc.	θ exp.	θ calc.	θ exp.	θ calc.
Min 1	0.33	0.08	0.28	0.06	0.25	0.06
Max 1	0.48	0.15	0.38	0.13	0.35	0.12
Min 2	0.77	0.44	0.48	0.37	0.50	0.35
Max 2	0.92	0.65	0.71	0.56		0.53
Min 3	1.22	1.04	0.89	0.90		0.87
Max 3	1.43	1.38	1.16	1.21		1.15
Min 4		1.86		1.66		1.61
Max 4		2.31		2.08		2.03

However, the first extrema could not be explained using the quoted Bohr potential. There was no ΔE function of exponential form which would give the right fit.

Also since the Bohr potential calculated by Lane and Everhart is known to be too flat in this collision range, we tried an unscreened exponential potential[27]) for the Ar_2 system. The Ar^+–Ar potential was obtained by subtraction of the orbital energy of the missing electron (Koopman's theorem). The ΔE function was empirically estimated by trial and error. A good fit as shown in table V was obtained

TABLE V

Calculated values for extrema at 3.5 keV together with the experimental results. θ^* was obtained by extrapolation of the values of Barat *et al.*[16])

	Experiment		Calculations				
	θ (deg)	θ^* (deg)	θ (deg)	L_g	L_u	$-(L_g - L_u)\theta$ (rad)	$2(\eta_{L_g} - \eta_{L_u})$ (rad)
Min 1	0.33		0.27	11271	11966	3.274	−0.118
Max 1	0.48		0.47	10396	11112	5.869	−0.250
Min 2	0.77	0.75	0.77	9599	10334	9.881	−0.468
Max 2	0.92	0.95	0.99	9185	9933	12.922	−0.637
Min 3	1.22	1.15	1.25	8797	9555	16.534	−0.844
Max 3	1.43	1.40	1.47	8524	9289	19.616	−1.025
Min 4		1.65	1.72	8256	9029	23.212	−1.229
Max 4		2.00	1.94	8050	8827	26.337	−1.415
Min 5		2.20	2.18	7847	8631	29.832	−1.614
Max 5		2.50	2.40	7678	8467	33.039	−1.799

with the following potentials:

$$V_{\Pi_g} = 10.150 \exp(-3.90r) + 16 - 22 \exp(-2.0r) \quad \text{(in eV)},$$
$$V_{\Pi_u} = V_{\Pi_g} + \Delta E, \quad \Delta E = 9000 \exp(r/0.24) \quad \text{(in eV)}. \tag{14}$$

These potentials are drawn in fig. 16. This fit was obtained at 3.5 keV primary energy. It must be remarked that the first minimum is of the right order of magnitude and the ΔE function is drastically larger than the one found by Barat *et al.*[16]) and Jones *et al.*[30]). A peculiar feature is also shown in table V: the distance between a minimum and a next maximum is smaller than the distance between a

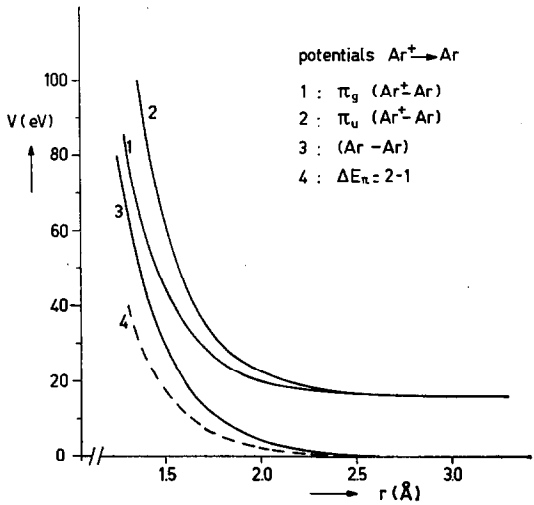

Fig. 16. Potentials for the (Ar^+–Ar) system which are used to calculate the relative elastic differential cross sections.

maximum and a next minimum. It is observed in the experiments as well as in our calculations. It is due to the fact that in eq. (12) the harmonic oscillation from the interference term is added to the negatively sloping background from the classical differential cross section. Note that the most important term in the argument of the cosine [eq. (12)], which causes the cross section to oscillate, is the $(L_u - L_g)\,\theta$ term. In other words, the existence of two different stationary L values. This justifies the use of the most refined orbital calculations.

If we use other potentials than eq. (14) the relative importance of $(L_u - L_g)\theta$ and $2(\eta_{L_g} - \eta_{L_u})$ is different. For instance, for the potentials (13) both terms are of the same order of magnitude.

As shown in table VI deviations occur from the experimental results. In order to fit the results at 1 keV one has to look for a ΔE function which is higher than

TABLE VI

Extrema for four primary energies (measurements and calculations). θ^* was obtained from Barat *et al.*[16])

	1 keV		3.5 keV			10 keV		15 keV	
	θ^* exp	θ calc.	θ exp.	θ^* exp.	θ calc.	θ exp.	θ calc.	θ exp.	θ calc.
Min 1		0.51	0.33		0.27	0.28	0.16	0.25	0.13
Max 1	0.60	0.89	0.48		0.47	0.38	0.27	0.35	0.22
Min 2	1.05	1.48	0.77	0.75	0.77	0.48	0.44	0.50	0.36
Max 2	1.45	1.90	0.92	0.95	0.99	0.71	0.57		0.46
Min 3	1.75	2.41	1.22	1.15	1.25	0.89	0.72		0.58
Max 3	2.10	2.84	1.43	1.40	1.47	1.16	0.84		0.68
Min 4	2.55	3.33		1.65	1.72		0.99		0.80
Max 4	3.00	3.76		2.00	1.94		1.11		
Min 5	3.40	4.24		2.20	2.18		1.25		
Max 5	3.80	4.66		2.50	2.40				
Min 6	4.10	5.13			2.64				

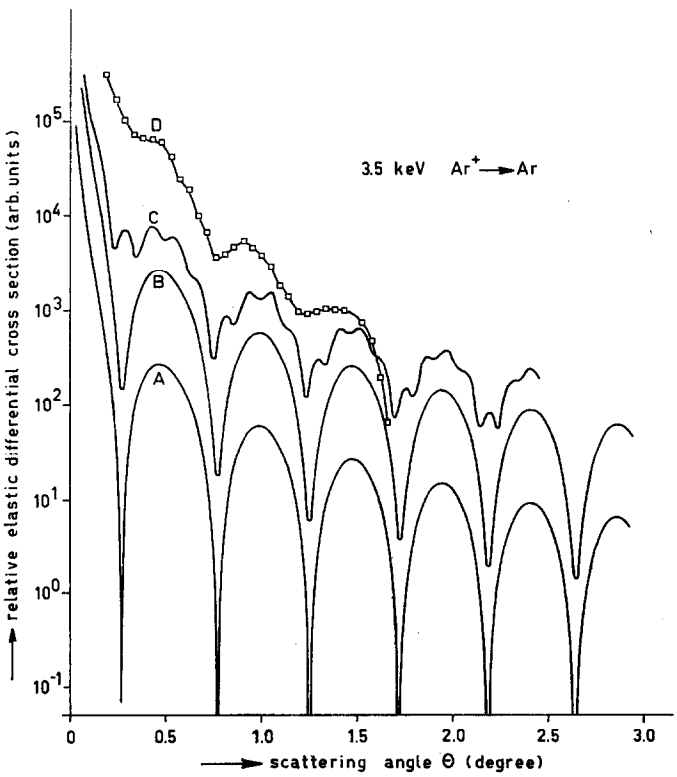

Fig. 17. Relative elastic differential cross section for $Ar^+ \rightarrow Ar$. A: calculated, taking only scattering of Π waves into account; B: σ convoluted with the angular resolution of the apparatus; C: calculated, taking Π and Σ scattering into account and convoluted with the angular resolution of the apparatus; D: experimental cross section.

the one we used but at 10 and 15 keV it must be lower. The conclusion is that ΔE and/or the potential are not exactly of the exponential form or that ΔE consists of two exponential expressions with different exponential constants.

In fig. 17 the calculated and measured cross sections are shown for $E_0 = 3.5$ keV. The theoretical function, curve A, was convoluted by our angular resolution of 4.6 min, giving curve B. The relative magnitudes of the extrema of curve B were corrected for the fact that Σ scattering contributes by about $\frac{1}{3}$ to the cross section.

We assumed that the Σ_g–Σ_u potential difference is a factor 3 larger than the Π_g–Π_u potential-energy difference. This is a very rough estimate. Indeed from fig. 17c one can see that the Σ oscillation which follows from this rough guess should be resolved by our apparatus. As this was not the case we may conclude that $\Delta E_\Sigma > 3\Delta E_\Pi$.

The effect of the introduction of Σ scattering brings the calculated depth of the minima more into line with the experimental depths.

The overall behaviour of the theoretical cross section in fig. 17c shows a slower decrease than the experimental curve with increasing θ. This deviation between experiment and theory can partly be explained by the fact that the calculations do not take into account the loss of particles into inelastic channels at larger scattering angles. At $\theta = 1.5$ deg about 75% of all particles are scattered inelastically (fig. 7). So the theoretical curve should be a factor 4 lower taking this effect into account.

5.3. Inelastic differential cross sections. The computer simulation of the orbit followed by the scattered particles enables us by means of a phase-shift method, to calculate the inelastic differential cross section.

In 5.1 it was mentioned that there are two potential surfaces on which the Ne^+ ion can move, which have the same final scattering angle and leave the target atom in the excited Ne ($2p^5$, 3s) state. This means that also in the inelastic channel an oscillating cross section as a function of the scattering angle can occur. In the calculations it is necessary to introduce a probability factor P giving the change for a transition from one adiabatic state to the other. This probability is given by the Landau–Zener formula [eqs. (7)]. A complication is that the particles scattered over θ following the (1.1.2) orbit have a different impact parameter and therefore a different radial velocity at r_c from the particles which are scattered over θ following the (1.2.2) orbit.

If we call orbit (1.1.2) A and (1.2.2) B, the differential cross section for inelastic scattering is given by

$$\sigma_{\text{inel}}(\theta) = |P_A^{\frac{1}{2}}(1 - P_A)^{\frac{1}{2}} f_A(\theta) + P_B^{\frac{1}{2}}(1 - P_B)^{\frac{1}{2}} f_B(\theta)|^2, \tag{15}$$

where $f_i(\theta)$ is given by formula (V. 3), ref. 28, p. 94 provided that the upper limit of the integral path is not ∞ but has a value determined by the r_c value. The differ-

ence between P_A and P_B can be considerable. $\partial/\partial r\,(H_{11} - H_{22})_{r=r_c}$ was found from the potentials 8 and 9 to be 80 eV/Å. H_{12} was estimated to be about 2 eV, which is about the average between the value found by Morgenstern[33]) for the corresponding crossing in Ar^+–Ar at $R_c = 1.4$ Å ($H_{12} \approx 1.3$ eV) and the value which can be found using the general dependence of H_{12} from R_c[34]) ($H_{12} \approx 3$eV).

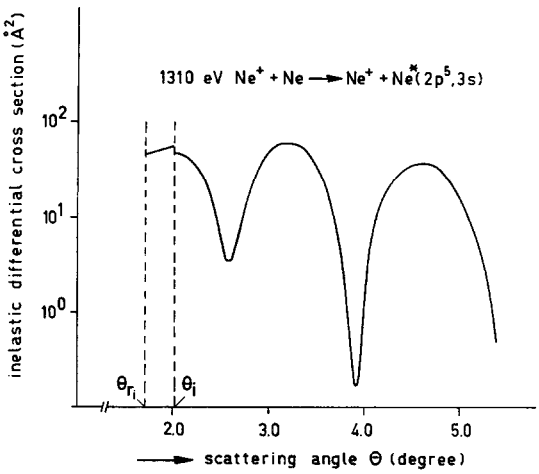

Fig. 18. Inelastic differential cross section of $Ne^+ + Ne \rightarrow Ne^+ + Ne^*$ ($2p^5$,3s) (calculated).

The resulting cross section for $\theta > 2^\circ$ is shown in fig. 18. Typical extrema are observed which are again extremely sensitive to the choice of the potential. Below $\theta = \theta_i$ from our θ–p plot (fig. 15) it can be seen that a situation occurs which is very similar to rainbow scattering. We therefore used the Airy function[31]) to calculate the cross section in that region. The fit at $\theta = \theta_i$ is good when one takes the uncertainty of H_{12} in consideration. The Airy function gives also a real cross section for $\theta < \theta_{r_i}$, the classical rainbow-scattering angle. In that region we did not proceed with the calculations because no radial velocity can be defined for these scattering angles. It must be stressed that the calculations were done using diabatic orbits which are not realistic in the crossing region.

6. *Conclusions.* 6.1. From the inelastic energy-loss spectra. 6.1.1. Ar^+–Ar. For each peak in the spectrum one or more families of excitations can be found which can explain the specific values of the inelastic-energy losses, reflected in that peak. A peak due to elastic collisions and a peak due to single-electron excitations can be identified unambiguously. A third and a fourth peak in the spectrum can be explained in several ways. It seems probable that collisions in which both, projectile and target atom, are excited contribute to the third peak.

The fourth peak may be due to collision processes in which the ion is excited and the target atom is excited to an auto-ionizing state. Especially with regard to the identification of the collision processes leading to the third and fourth peaks, high-resolution Q measurements in coincidence with final charge of the target atom are required.

6.1.2. Ne^+–Ne. For τ values $\leqslant 10$ keV deg, the three observed peaks can be explained in a similar way as all Ar^+–Ar spectra, *i.e.*, by excitations in one or both collision partners. For instance, a small peak is resolved with $Q = 16.7$ eV corresponding to excitation of the neon target atom to the first excited state.

For τ values $\geqslant 10$ keV deg, the two inelastic peaks shift with increasing τ values towards larger Q values, even through the limits set by the explanation in the lower τ region. Two more or less unsatisfactory explanations are offered in the case of the first inelastic peak. 1) A gradual change of excitation of the target alone ($Q \simeq 19$ eV), *via* projectile alone ($Q \geqslant 27$ eV) to excitation of both collision partners ($Q \approx 50$ eV). 2) A transition of the target atom into the first ionization continuum. In either of the two explanations the question remains why in the case of Ar^+ on Ar no shifting of the inelastic peak occurs. Similar calculations which have led to the direct-ionization hypothesis for $Ne^+ \rightarrow Ne$[25]) should be performed for $Ar^+ \rightarrow Ar$. On the experimental side, measurements with larger energy resolution could shed light on the problem of shifting peaks.

A small peak is resolved with a Q value of 23.4 eV. No excitation can possibly explain this peak. It may be due to the supposed direct ionization and should, in that case, indicate that electrons with a most probable energy of ± 2 eV are formed.

6.2. From the calculations and experimental cross sections. It is not valid to determine a curve-crossing point of the ground-state and an excited-state potential using a relation between τ and the impact parameter based upon the ground-state potential alone. The collision should be described through a complex potential. The error due to not taking a complex potential can be as large as 10%.

The oscillations in the elastic differential cross section of $Ar^+ \rightarrow Ar$, due to the interference of the waves scattered over a Π_g and a Π_u potential and over a Σ_g and Σ_u potential can be very well described by the semi-quantum treatment. The stationary values of both waves leading to the same scattering angle and the phase shifts are calculated assuming a classical orbit. It is shown that this classical calculation has to take into account the fact that there are four different orbits leading to the same scattering angle. A perfect fit can be obtained for the 3.5 keV $Ar^+ \rightarrow Ar$ measurement using an exponential potential for the Π_g and Π_u potential. This is impossible with any screened Coulomb potential. For other primary energies deviations occur. It might be possible to solve this by using a screened potential in which the screening constant can have several values, as a function of distance.

Calculations show that oscillations can be expected in the differential inelastic cross sections due to one well-defined single excitation. The natural continuation of the "collision spectroscopy" seems therefore a combination of *ab initio* calculations of the energy values of the excited pseudo-molecule and energy-loss measurements with such resolution that the different components in one peak can be resolved. Coincidence measurements of the scattered particles with photon emission might be helpful in this respect.

Acknowledgements. The authors are indebted to Professor J. Los for many helpful discussions and his comments on the manuscript.

This work is part of the research programme of the Stichting voor Fundamenteel Onderzoek der Materie (Foundation for Fundamental Research on Matter) and was made possible by financial support from the Nederlandse Organisatie voor Zuiver-Wetenschappelijk Onderzoek (Netherlands Organisation for the advancement of Pure Research).

REFERENCES

1) Morgan, G.H. and Everhart, E., Phys. Rev. **128** (1962) 667.
2) Afrosimov, V.V., Gordeev, Yu.S., Panov, M.N. and Federenko, N.V., Zh. Tekh. Fiz. **34** (1964) 1613; **34** (1964) 1624; **34** (1964) 1637; **36** (1966) 123; [Soviet Physics–Techn. Phys. **9** (1965) 1248; **9** (1965) 1256; **9** (1965) 1265; **11** (1966) 89].
Afrosimov, V.V., Gordeev, Yu.S., Polyanskii, A.M. and Shergin, A.P., Zh. eksper. teor. Fiz. **57** (1969) 806; [Soviet Physics–JETP **30** (1970) 441].
3) Kessel, Q.C. and Everhart, E., Phys. Rev. **146** (1966) 16.
4) Kessel, Q.C., McCaughey, M.P. and Everhart, E., Phys. Rev. **153** (1967) 57.
5) Flinchbaugh, D.E., J. chem. Phys. **43** (1965) 910.
6) Fastrup, B., Hermann, G. and Smith, K.J., Phys. Rev. **3** (1971) 1591.
7) Bingham, F.W., Phys. Rev. **182** (1969) 180.
8) Knystautas, E.J., Kessel, Q.C., DelBoca, R. and Hayden, H.C., Phys. Rev. **1** (1970) 825.
Hayden, H.C. and Knystautas, E.J., Phys. Rev. **3** (1971) 206.
9) Kessel, Q.C., Rose, P.H. and Grodzins, L., Phys. Rev. Letters **22** (1969) 1031.
10) Fano, U. and Lichten, W., Phys. Rev. Letters **14** (1965) 627.
11) Lichten, W., Phys. Rev. **164** (1967) 131.
12) Lorents, D.C. and Aberth, W., Phys. Rev. **139** (1965) 1017.
13) Aberth, W. and Lorents, D.C., Phys. Rev. **144** (1966) 109.
14) Smith, F.T., Marchi, R.P., Aberth, W. and Lorents, D.C., Phys. Rev. **161** (1967) 31.
15) Baudon, J., Barat, M. and Abignoli, M., J. Phys. **B1** (1968) 1083; **3** (1970) 207.
16) Barat, M., Baudon, J., Abignoli, M. and Houver, J.C., J. Phys. **B3** (1970) 230.
17) McCaroll, R. and Piacentini, R.D., Proc. VII ICPEAC (1971) p. 133.
18) Lorents, D.C. and Conklin, G., Proc. VII ICPEAC (1971) p. 130.
19) Afrosimov, V.V., Gordeev, Yu.S., Lavrov, V.M. and Nikulin, V.K., Proc. VII ICPEAC (1971) p. 143.
20) Bierman, D.J. and Turkenburg, W.C., Phys. Rev. Letters **25** (1970) 633.
21) Snoek, C., thesis, Amsterdam (1966).
22) Van Eck, J., De Heer, F.J. and Kistemaker, J., Physica **30** (1964) 1171.

23) Bierman, D.J., Turkenburg, W.C. and Bhalla, C.P., Physica **60** (1972) 357.
24) Lehmann, C. and Leibfried, G., Z. Phys. **172** (1962) 465.
25) Thulstrup, E.W. and Johansen, H., Phys. Rev. **A6** (1972) 206.
26) Landau, L., Physik. Z. Sowjetunion **2** (1932) 46; Stückelberg, E.C.G., Helv. phys. Acta **5** (1932) 369; Zener, C., Proc. Roy. Soc. **A137** (1932) 696; Bates, D.R., *ibid.* **A257** (1960) 22.
27) Smith, F.T., Phys. Rev. **A5** (1972) 1708.
28) Bernstein, R.B., Molecular Beams, J. Ross, ed., John Wiley and Sons Inc. (New York, 1966).
29) Marchi, R.P. and Smith, F.T., Phys. Rev. **139** (1965) 1025.
30) Jones, P.R., Eddy, N.W., Gilman, H.P., Jhaveri, A.K. and Van Dijk, G., Phys. Rev. **147** (1966) 76.
31) Kotova, L.P. and Ovchinnikova, M.Ya., Proc. VII ICPEAC (1971), p. 123.
32) Bierman, D.J., thesis, Amsterdam (1972).
33) Morgenstern, R., thesis, Freiburg (1971).
34) Hasted, J.B., Physics of Atomic Collisions, Butterworths (London, 1964) 443.